JMEPEG (2016) 25:1426–1435
DOI: 10.1007/s11665-016-1983-x


1059-9495/$19.00

# Degradation of SPS-Fabricated YSZ and $Nd_2O_3$-YSZ Ceramics in Supercritical Water

*A. Siebert-Timmer and L. Bichler*

*(Submitted October 7, 2015; in revised form January 14, 2016; published online March 3, 2016)*

**Zirconia ($ZrO_2$) ceramics are being considered as a candidate material for thermal insulating barriers in pressure tubes used in the supercritical water (SCW) nuclear reactors. However, the literature suggests that zirconia may undergo a detrimental phase transformation which is accelerated in aqueous environments. In this research, 8 mol% Yttria-Stabilized Zirconia (YSZ) ceramics with the addition of 5 and 10 mol% $Nd_2O_3$ were manufactured via spark plasma sintering (SPS) process and subsequently subjected to a SCW environment. The weight losses and microstructural evolutions of these materials during SCW exposure were studied. The results suggest that doping YSZ with $Nd_2O_3$ significantly decreased the degradation rate of the YSZ ceramic and improved its structural stability. X-ray diffraction studies revealed that after degradation testing, the $Nd_2O_3$ helped to retain the desirable cubic phase of YSZ matrix. In the case of pure YSZ ceramic, a phase change of the matrix toward the monoclinic lattice was observed and likely contributed to the ceramic's disintegration in SCW environment.**

**Keywords** degradation, neodymium oxide, $Nd_2O_3$, spark plasma sintering, supercritical water, zirconia, $ZrO_2$

## 1. Introduction

At temperatures and pressures above 374 °C and 22.1 MPa, respectively, water enters the supercritical water (SCW) phase and exhibits a very high diffusivity and enthalpy (Ref 1). As a result, there has been a great interest in using supercritical water as a coolant in the next generation of nuclear reactors (Generation IV Supercritical Water Reactors (SCWRs)) (Ref 2, 3). However, the required high temperatures and pressures of the supercritical water coolant along with strong doses of radiation result in an exceptionally aggressive environment, which poses unique challenges for current nuclear materials, as well as any new potential materials (Ref 4).

Zirconia ($ZrO_2$) ceramics have been identified as a candidate material for thermal insulation barriers in SCWR components (Ref 5). For example, one potential application is the placement of a zirconia liner to protect a zirconium alloy pressure tube from thermally induced creep and deformation during reactor operation (Ref 5). Zirconia ceramics are attractive for such applications mainly due to their low thermal conductivity, good chemical inertness, and neutron transparency. At room temperature, zirconia has a monoclinic crystal structure which favors a sevenfold oxygen coordination number. Often referred to as Baddeleyite, the formation of this monoclinic crystal structure is attributed to the large ionic size difference between the $Zr^{4+}$ and $O^{2-}$ ions (Ref 6, 7). Upon heating, the monoclinic structure transforms to a tetragonal lattice at temperatures above 1100 °C and to a cubic lattice above 2370 °C (Ref 4, 6). It has been found that, at these higher temperatures, the tetragonal and cubic polymorphs favor a more symmetric eightfold oxygen coordination number, which strains the cation network due to oxygen overcrowding and ultimately, volumetric changes in the volume of the unit cell (Ref 8). The tetragonal and cubic polymorphs are often stabilized at room temperature by doping the zirconia matrix with either di- or tri-valent ions (e.g., $Ca^{2+}$, $Y^{3+}$) (Ref 7). During stabilization, the added cations substitute for the $Zr^{4+}$ ions in the lattice and, to maintain electrostatic neutrality, generate oxygen vacancies in the sublattice (Ref 6). It has been found that it is the generation of these oxygen vacancies, which controls the room-temperature phase stabilization of tetragonal and cubic zirconia rather than the substitutional dopant cations (Ref 9, 10). Li et al. (Ref 8) explained the mechanism of stabilization in terms of the relief of the internal strain of zirconia's higher-temperature polymorphs. By introducing oxygen vacancies, the effects of oxygen overcrowding are reduced, and the internal strain in the $Zr^{4+}$ cation lattice is relieved, allowing for room-temperature stabilization (Ref 8). Several types of the stabilized zirconia systems with low valence dopants have been studied in the literature (Ref 6, 8, 9, 11). It has been found that in addition to the required low valence and high solid solubility in zirconia, suitable dopant cations must also have an ionic radius larger than that of $Zr^{4+}$ ions (0.84 Å) (Ref 12). These constraints limit the number of suitable dopants to trivalent rare-earth oxides. However, less-expensive divalent additives such as CaO and MgO have also been found to be able to stabilize the higher-temperature polymorphs of zirconia (Ref 6, 11).

Once stabilized, the zirconia phases exhibit attractive toughness and ionic conductivity properties (Ref 7, 13-15). However, despite these enhanced properties, the stabilized zirconia ceramics have been found to exhibit a degradation behavior when exposed to humid environments. Typically, degradation of the stabilized zirconia involves the transformation of the stabilized phase back to the monoclinic polymorph, with a concomitant and significant volume expansion (~7%) leading to material cracking and, ultimately, component failure (Ref 15). The rate of this degradation behavior is affected by a

**A. Siebert-Timmer** and **L. Bichler**, School of Engineering, University of British Columbia – Okanagan, 3333 University Way, Kelowna V1V 1V7, Canada. Contact e-mail: lukas.bichler@ubc.ca.

variety of factors including the grain size and porosity (Ref 16, 17), chemical composition of the ceramic, and the environment (e.g., pH and oxygen content) (Ref 18). Furthermore, it has been reported that the cubic-stabilized zirconia outperforms tetragonal-stabilized zirconia ceramics in humid environments (Ref 19, 20). The literature suggests that this detrimental behavior is due the annihilation of oxygen vacancies by water molecules ($H_2O$). Guo et al. (Ref 21) proposed sequential degradation mechanism starting with the chemical absorption of $H_2O$ on the surface followed by the reaction of $H_2O$ with surface $O^{2-}$ molecules forming hydroxyl groups of $OH^-$. These $OH^-$ ions then diffuse into the matrix resulting in the annihilation of oxygen vacancies. The changes in oxygen vacancy concentration result in monoclinic transformation and formation of both micro and macrocracks, which expose new surfaces allowing further degradation. Many experimental observations support the proposed oxygen vacancy-annihilation mechanism (Ref 21-23). Despite these studies, the exact mechanism of the degradation process of the stabilized zirconia ceramics remains widely debated, and there has been a limited progress in controlling the degradation behavior.

Reported studies suggest that the degradation of the stabilized zirconia ceramics in aqueous solutions may be influenced by doping the stabilized zirconia matrix with a secondary additive. The available literature describes the ability to reduce the degradation rate of the YSZ by co-stabilizing the matrix with rare-earth oxides such as Neodymium Oxide ($Nd_2O_3$) (Ref 24, 25). In addition, studies also suggest that degradation rates can be hindered through grain refinement, which can be obtained through specialized processing techniques such as spark plasma sintering (SPS) (Ref 16, 17). SPS is a rapid sintering process which can fabricate high-density materials with processing times up to 20 times faster than conventional sintering techniques. This rapid sintering enables tight control of grain growth, thus allowing for the fabrication of highly dense nanocyrstaline materials (Ref 26). In this work, SPS processed cubic 8 mol% Yttria-Stabilized Zirconia (YSZ), as well as YSZ ceramics codoped with 5 and 10 mol% $Nd_2O_3$ were subjected to static SCW degradation testing at 400 °C and 31 MPa. Degradation rates as well as the microstructure and phase evolution of the sintered samples during SCW exposure were subsequently evaluated.

## 2. Experimental Procedure

### 2.1 Experimental Materials

Precursor nanopowders of the 8 mol% Yttria-Stabilized Zirconia (YSZ) and Neodymium Oxide ($Nd_2O_3$) were obtained from Inframat Advanced Materials, USA (product #4039OR-8601 and #60N0801, respectively). The initial particle sizes for the YSZ and $Nd_2O_3$ powders ranged between 30 and 60 nm and 80 and 110 nm, respectively. Powder blends of YSZ with the addition of 5 and 10 mol% $Nd_2O_3$ were prepared by mixing the constitutive powders in a beaker with MeOH for 2 h using a magnetic stirrer, followed by drying for 24 h at room temperature.

### 2.2 Spark Plasma Sintering

Spark plasma sintering (SPS) of the blended $Nd_2O_3$-YSZ powders was carried out using a Thermal Technology spark plasma sintering machine (10-3 model). For each sintered ceramic, 10 g of the powder blend was placed in a graphite die lined with Grafoil® sheet. The SPS consolidation process involved simultaneous heating and pressing of the sample until the desired sintering temperature was reached, followed by temperature and pressure hold at the sintering condition. Thereafter, the sintering pressure was released, and the material was allowed to cool in the SPS machine. The sintering parameters for the different composites are summarized in Table 1. As can be seen from Table 1, it was necessary to adjust the sintering temperature and pressure for the studied compositions in order to produce solid disks which did not fracture upon ejection from the sintering die and retain a relative density $>90\%$. All the sintered disks had a 20-mm diameter and a $\sim$4-mm thickness. The surfaces of the as-sintered ceramics had a gray coloration rich in carbon, which was attributed to the diffusion of carbon from the graphite tooling during SPS processing (Ref 27-29).

### 2.3 Characterization

A Tescan MIRA$^3$ XMU Scanning Electron Microscope (SEM) with an Oxford X-max x-ray Energy Dispersive Spectroscope (XEDS) detector was used for imaging and chemical analysis (without ZAF correction). Microstructure analysis was performed on the representative as-sintered samples polished with SiC papers followed by diamond paste polishing. To reveal the grain structure of the sintered specimens, thermal etching in air was performed for 1 h at a temperature 50 °C below the corresponding sintering temperature. The grain size was then measured via Buehler OmniMet image analysis software using the linear intercept method. The density of the as-sintered materials was determined using the Archimedes' principle. To study the phases present in the sintered materials before and after SCW degradation testing, x-ray diffraction (XRD) analysis was performed using a Bruker D8 Advanced-ray Diffractometer in Bragg-Brentano configuration with a Lynxeye silicon strip detector. Diffraction peak measurements were performed using Cu-K$\alpha$ radiation (40 mA, 40 kV) for all samples.

After SCW degradation testing, the surfaces of the samples were polished with a 600 grit SiC paper, and their microstructures were reexamined. Also, Inductively Coupled Plasma-Mass Spectroscopy (ICP-MS) was performed on the solutions

**Table 1 Processing conditions, relative density, and grain size of the as-sintered YSZ and $Nd_2O_3$-YSZ ceramics**

| Composition | Pressure, MPa | Temperature, °C | Dwell time, min | Relative density (a), % | Grain size (a), μm |
|---|---|---|---|---|---|
| YSZ | 30 | 1400 | 7 | $95.6 \pm 1.1$ | $9.84 \pm 0.53$ |
| 5 mol% $Nd_2O_3$-YSZ | 40 | 1400 | 5 | $91.8 \pm 0.01$ | $2.37 \pm 0.21$ |
| 10 mol% $Nd_2O_3$-YSZ | 40 | 1300 | 5 | $92.3 \pm 0.1$ | $0.83 \pm 0.05$ |

(a) Error shown taken from a 95% confidence interval

retrieved from the SCW vessels to determine the presence of dissolved species in the solutions. ThermoFisher Element XR ICP-MS was used on 0.1 mL of solution diluted 1000 times in nanopure water containing 1% of trace-grade nitric acid and 1.0 ppb of Indium as the internal standard. Sample results were averaged from interpolation data obtained from three passes of each sample, and then corrected for the dilution factor.

### 2.4 Supercritical Water Degradation Testing

As-sintered disks were sectioned to $\sim 4 \times 4 \times 4$ mm cubes using a diamond wafer saw and polished with a 600 grit SiC paper, followed by ultrasonic cleaning in distilled water for 5 min. The SCW degradation testing was performed by placing one sectioned cube along with 20 mL of distilled water into a 316L stainless steel vessel sealed with Swagelok® caps at each end. These test vessels were designed according to *ASTM G31* (Ref 30) and had a length of 254 mm (10 in.), outer diameter of 25.4 mm (1 in.), and a wall thickness of 3.05 mm (0.120 in.). The sealed vessels were placed horizontally in a furnace and heated to 400 °C at a heating rate of 2.6 °C/min. Based on the thermodynamic equations of state, at 400 °C the internal pressure in the vessel reached 31 MPa indicating the supercritical state had been reached. These environmental conditions caused the ionic product of the distilled water to drop to $10^{-15}$ mol$^2$ L$^{-2}$ which correlated to an increase in pH from 7 to 7.5. Therefore, the defined dwell conditions resulted in a slightly basic test medium. After a dwell time of 2.5 h at 400 °C, the furnace was switched off and the samples were allowed to furnace cool. The vessels were removed from the furnace once the temperature reached below 60 °C (after ~17 h). This controlled cooling procedure was necessary to ensure that no water evaporated upon opening the vessels after a test (the maximum water loss was $< 2$ mL). Degradation testing was repeated three times for each ceramic composite. Weight losses of the tested samples were then recorded, and the respective degradation rates ($r$) were calculated according to Eq 1 (Ref 29).

$$r = (K * W)/(A * t * D) \quad \text{(Eq 1)}$$

where $W$ was the final weight loss in g, $A$ was the initial surface area of the sectioned cube in cm$^2$, $D$ was the measured density in g/cm$^3$ and $t$ was the total time of exposure in hours. Parameter $K$ was the unit conversion constant which, for the calculated degradation rate to be expressed in mm/year, was equal to $8.76 \times 10^4$.

## 3. Results and Discussion

### 3.1 Densification

The sintering temperature and pressure were adjusted as $Nd_2O_3$ was added to YSZ in order to avoid sample cracking upon ejection from the sintering die, as well as to maintain the relative density of the as-sintered ceramic between 90 and 95%. At this density level, the thermal insulating properties were optimal (results not reported here). The SPS process optimization experiments clearly demonstrated that the sintering pressure and sintering temperature influence the relative density of ceramics. For example, a 10 MPa pressure increase resulted in an increase in the relative density of pure 8 mol% YSZ ceramic by 9% (Ref 31), while the temperature had a lesser effect at sintering temperatures above 1300 °C (Ref 32). The relative density and grain size of the materials sintered in this work are summarized in Table 1. With respect to the plain YSZ ceramic, the additions of the 5 and 10 mol% $Nd_2O_3$ significantly reduced the matrix grain size, while only slightly (~3 to 5%) reducing the relative density. It is important to note that, even with the higher sintering pressure, the relative density of the $Nd_2O_3$ ceramics decreased. As a result, $Nd_2O_3$ addition was seen to hinder densification during the processing of the YSZ composite ceramics. Detailed micrographs of the grain structure for the various sintered ceramics are presented in section 3.4.

The general microstructure of the as-sintered ceramics is provided in Fig. 1. The microstructure of the YSZ contained uniformly distributed microporosity. In the case of the $Nd_2O_3$-containing ceramics, XEDS scans revealed large Nd-rich regions within the matrix [marked with arrows in Fig. 1(b) and (c)]. At the 10 mol% addition level, the agglomerations formed distinct bands. Although extensive powder-blending process was carried out in an effort to minimize segregation of

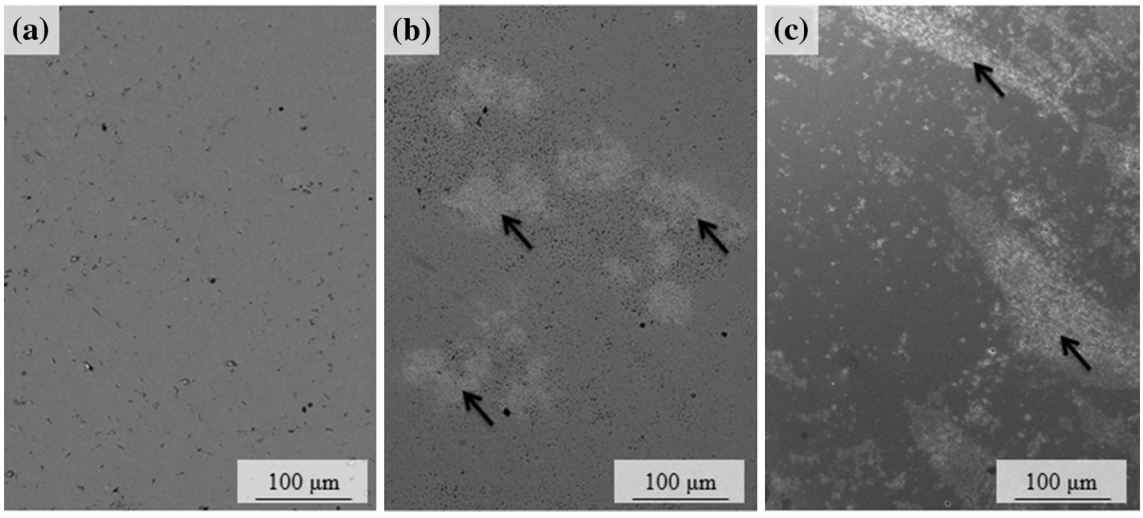


**Fig. 1** General microstructures of the as-sintered ceramics: a) YSZ, b) 5 mol% $Nd_2O_3$-YSZ, and c) 10 mol% $Nd_2O_3$-YSZ. Arrows indicate Nd-rich areas

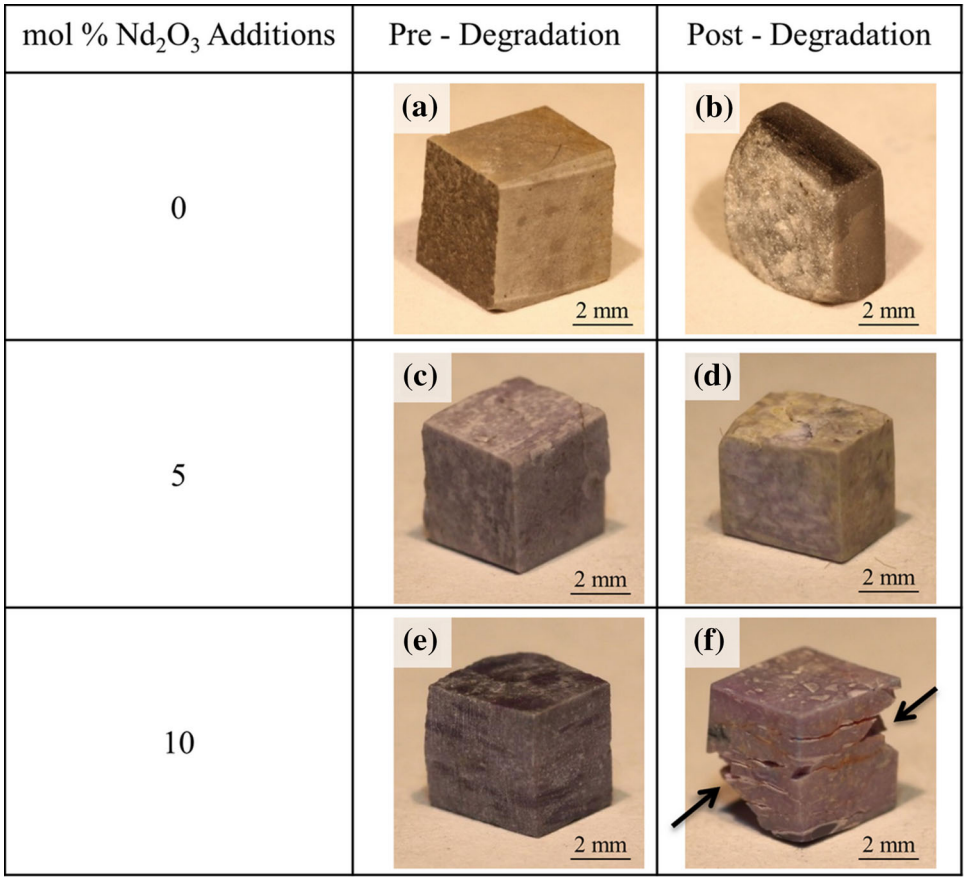


**Fig. 2** Specimens of ceramic composites before and after supercritical water degradation testing. Arrows indicate spalled surfaces

**Table 2 Calculated weight losses and degradation rates for the YSZ and $Nd_2O_3$-YSZ ceramics**

| Composition | Sample number | Weight loss, g | Degradation rate, mm/year | Comments |
|---|---|---|---|---|
| YSZ | 1 | 0.1923 | 120 | Preferential degradation |
| | 2 | 0.3994 | 260 | Disintegrated |
| | 3 | 0.1704 | 166 | Disintegrated |
| 5 mol% $Nd_2O_3$-YSZ | 1 | 0.0020 | 1.67 | Intact |
| | 2 | 0.0022 | 1.49 | Intact |
| | 3 | 0.0018 | 1.35 | Intact |
| 10 mol% $Nd_2O_3$-YSZ | 1 | 0.0124 | 10.10 | Cracking and spallation |
| | 2 | 0.0036 | 2.76 | Cracking and spallation |
| | 2 | 0.0249 | 17.80 | Cracking and spallation |

the $Nd_2O_3$ in the YSZ matrix, fully homogeneous powders and the as-sintered structures were not possible to achieve. Similar observations were reported by Verdon (Ref 33) where $Er_2O_3$ and YSZ powders were blended using a planetary ball mill (Fritsch Pulverisette 7) in a wet medium. The ball milling results were comparable to those observed with $Nd_2O_3$, with the formation of agglomerates and bands in both blending techniques. These results suggest that regardless of the blending technique used, mixtures containing rare-earth dopant amounts above 5 mol% will likely exhibit a heterogeneous structure.

### 3.2 Degradation Rates

Representative images of the sectioned specimens before and after degradation testing are provided in Fig. 2. The measured weight losses and the calculated degradation rates for each specimen are provided in Table 2.

Pure YSZ ceramic specimens were seen to frequently fail and disintegrate during exposure to supercritical water (two out of the three tested specimens disintegrated completely). In comparison, the $Nd_2O_3$-YSZ ceramics exhibited both an improved stability and significantly lower degradation rates.

In comparison, the 5 mol% $Nd_2O_3$-YSZ ceramic samples, the 10 mol% $Nd_2O_3$-YSZ samples exhibited higher degradation rates, which was attributed to a cracking and spallation of the samples, as seen in Fig. 2(f). SEM analysis revealed that the cracks present in the ceramic sample after degradation testing often propagated lengthwise through the large Nd-rich bands found in the ceramic's interior. SEM images of the Nd-rich bands before and after degradation testing are shown in Fig. 3,

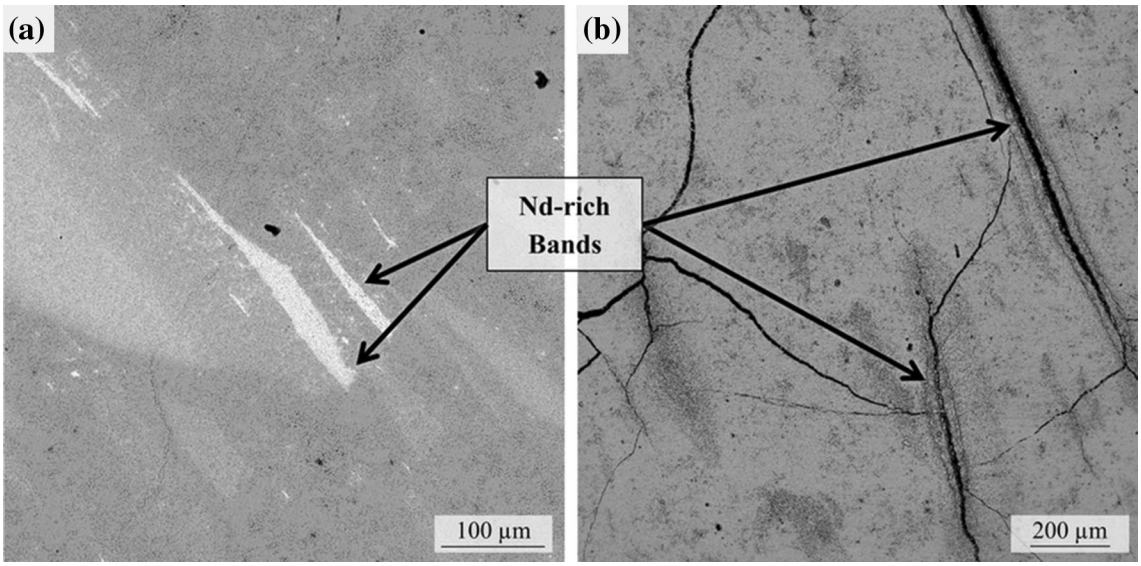


**Fig. 3** Nd-rich bands in the 10 mol% $Nd_2O_3$-YSZ ceramic a) before and b) after degradation testing

and suggest that the banding contributed to crack initiation and propagation during degradation testing. At room temperature, $Nd_2O_3$ has a hexagonal structure with thermal expansion coefficients of $6.9 \times 10^{-6}$ $K^{-1}$ and $14.7 \times 10^{-6}$ $K^{-1}$ in the *a*- and *c*-axis, respectively, while cubic YSZ has an expansion coefficient of $7.6 \times 10^{-6}$ $K^{-1}$ (Ref 34, 35). Thus, at room temperature, the thermal expansion along the *c*-axis of $Nd_2O_3$ is nearly double the thermal expansion of 8 mol% YSZ. In addition, these coefficients increase nonlinearly with the increasing temperature. Compared to room temperature, at ~400 °C, the $Nd_2O_3$ thermal expansion coefficient along the *a*-axis increases by 33%, while the thermal expansion coefficient along the *c*-axis increases by 7% (the thermal expansion coefficient for the YSZ matrix increases by 22%) (Ref 34, 35). Therefore, during heating and cooling, the differences in thermal expansions behavior between Nd-rich bands and the cubic zirconia matrix likely promoted the nucleation of cracks. In the case of the 5 mol% $Nd_2O_3$-YSZ ceramic, the microstructure was relatively homogeneous, and thus crack formation in the vicinity of Nd-rich agglomerations was not observed. It is important to note that cracking and spallation were only observed after SCW degradation testing and not after thermal etching the as-sintered ceramics in air (which was performed to reveal grain boundaries). This result suggests that the applied pressure and SCW contributed to this observed spallation behavior in addition to the thermal mismatch between the matrix and the Nd-rich bands.

### 3.3 Phase Evolution

XRD analysis of the SPS as-sintered ceramics revealed that the YSZ matrix remained cubic, without any undesirable lattice transformation toward the tetragonal or monoclinic phase. However, in comparison to the pure YSZ ceramics, a distinct lattice shift was observed in the $Nd_2O_3$ containing composites, suggesting that $Nd^{3+}$ ions were diffusing into the YSZ lattice during sintering (the ionic radii for $Zr^{4+}$, $Y^{3+}$ and $Nd^{3+}$ ions are 0.84, 1.019, and 1.109 Å, respectively) (Ref 36). This was further confirmed via lattice parameter measurement where, compared to the as-sintered YSZ ceramic, $Nd_2O_3$ additions of 5 and 10 mol% increased the lattice parameter by 0.6 and 1%, respectively (Table 3).

**Table 3 Lattice parameter measurements for the YSZ and $Nd_2O_3$-YSZ ceramics before and after degradation testing**

| Composition | Lattice parameter, Å (a) Predegradation | Post-degradation |
|---|---|---|
| YSZ | 5.1274 | $a_t$ = 5.1390 (b)<br>$c_t$ = 3.6263 (b) |
| 5 mol% $Nd_2O_3$-YSZ | 5.1622 | 5.1614 |
| 10 mol% $Nd_2O_3$-YSZ | 5.1793 | 5.1809 |

(a) Cubic lattice ($a_c$) unless otherwise noted
(b) Tetragonal lattice ($a_t$,$c_t$)

In addition to the YSZ matrix's cubic peaks, a secondary phase was detected in the XRD plots (Fig. 4a), and was associated with the formation of a ZrC phase. These carbides were likely the result of diffusion of carbon from the graphite tooling into the ceramic during SPS processing. Such diffusion has been reported by other researchers earlier (Ref 26-28). No secondary phases were observed in the Nd containing ceramics, as shown in Fig. 4(b) and (c), suggesting that these ceramics had a relatively homogenous matrix and the Nd-rich agglomerates as well as bands observed in the as-sintered ceramics had a relatively low volume fraction. In the case of the 10 mol% $Nd_2O_3$-YSZ ceramic (Fig. 4c), the XRD plots suggested the presence of a minor phase: however, this could not be indexed at statistically relevant level.

After SCW degradation testing, a slight peak shift was observed in the pure YSZ sample as shown in Fig. 4(a) which suggested that the stabilized cubic system transformed into a tetragonal system. The measured cubic and tetragonal lattice parameters for the pure YSZ ceramic closely corresponded to values reported in the literature (Ref 37, 38). In the case of the $Nd_2O_3$-YSZ ceramics, their lattices remained stable after exposure to SCW, as seen in Table 3. Furthermore, both the ZrC and

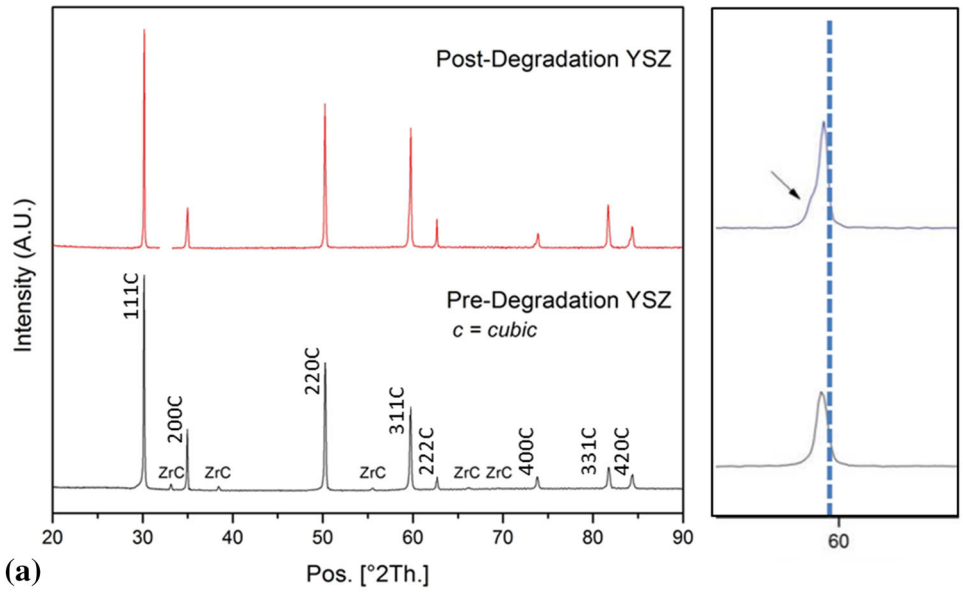


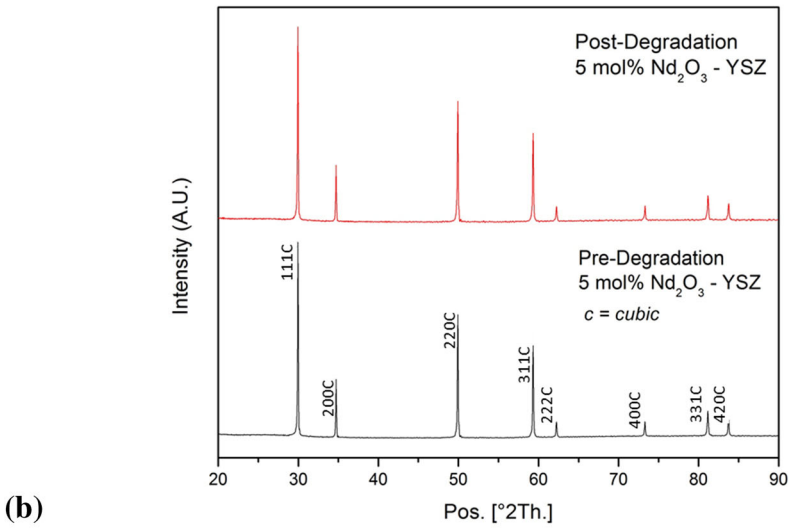


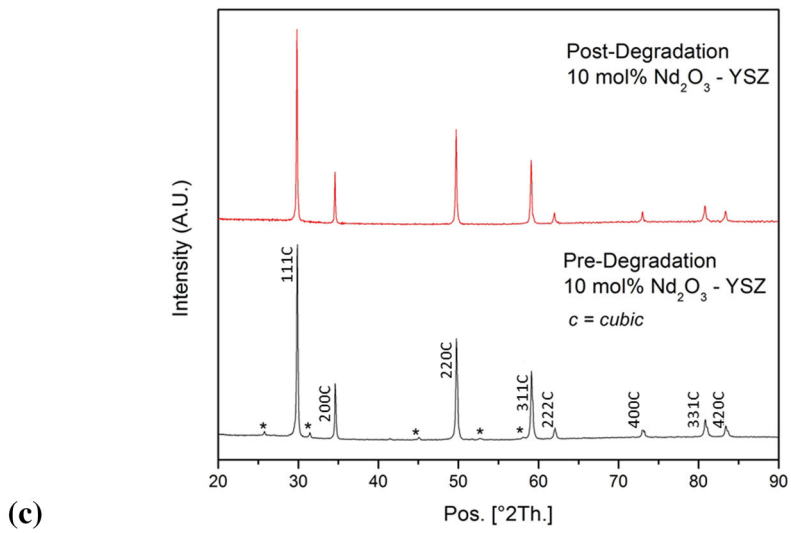


**Fig. 4** XRD plots for SPS ceramic composites before and after degradation testing. a) pure YSZ, b) 5 mol% $Nd_2O_3$-YSZ, and c) 10 mol% $Nd_2O_3$-YSZ with (*) peaks indicating an unknown trace phase

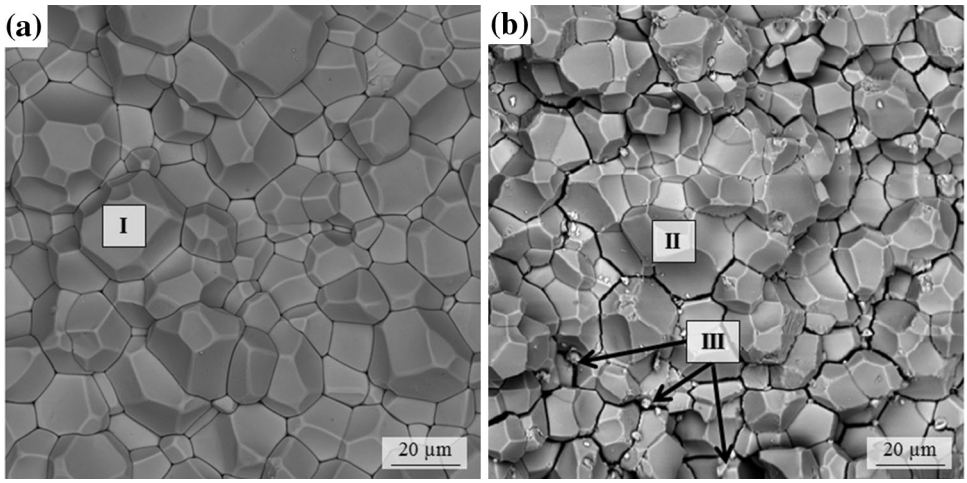


**Fig. 5** SEM micrograph of the pure YSZ ceramic a) before and b) after degradation testing

**Table 4 Chemical analysis of the pure YSZ ceramic**

| Sample | Region | Composition (a) mass% | | | | |
|---|---|---|---|---|---|---|
| | | Zr | O | Y | Hf | Cl |
| YSZ | Theoretical | 63.7 | 25.3 | 11.0 | … | … |
| | I | 64.1 ± 0.5 | 25.2 ± 3e−2 | 9.3 ± 0.4 | 1.5 ± 0.3 | 0.0 ± 3e−2 |
| | II | 64.1 ± 0.7 | 25.2 ± 0.1 | 8.9 ± 0.3 | 1.8 ± 0.8 | 0.0 ± 2e−2 |
| | III | 73.1 ± 0.2 | 25.8 ± 2e−2 | 0.1 ± 0.1 | 1.0 ± 0.2 | 0.0 ± 0.0 |

(a) Error shown taken from the standard deviation

the unknown phase observed in the as-sintered ceramics were absent in the XRD scans performed after SCW testing.

### 3.4 Microstructure Evolution

The general microstructure of the YSZ ceramic before and after degradation testing exhibited a homogenous matrix, as shown in Fig. 1(a) earlier, and in more detail in Fig. 5. The fracture surface of the YSZ ceramic after testing is shown in Fig. 5(b), and clearly shows the grain structure of the ceramic. SEM-XEDS scans revealed that the levels of the primary solutes in the as-sintered YSZ were in good agreement with the expected theoretical values, as seen in Table 4 (region 'I'). After degradation testing, the matrix composition remained close to the theoretical values, as shown in Table 4 (region 'II'). Despite the chemical similarity, grain pull out was observed on the surface of the degraded specimens. In addition, small particles were observed on the spalled surfaces of the degraded YSZ samples, as indicated by region 'III' in Fig. 5. Chemical analysis revealed that these particles had a composition consistent with pure $ZrO_2$ (74 mass% Zr and 26 mass% O). These observations suggest that during SCW, progressive transformation of the cubic phase toward the tetragonal and monoclinic phases likely occurred, as was also observed during XRD analysis. Interestingly, the XRD analysis did not detect monoclinic zirconia phase in the degraded YSZ samples. This was likely the result of absence of the monoclinic $ZrO_2$ on the spalled surfaces of YSZ, since the phase transformation from the cubic or tetragonal to the monoclinic phase is associated with ~7% volume expansion, which would effectively eject the transformed monoclinic grains from the surface, leaving behind voids. Consequently, the volume fraction of the monoclinic phase on the spalled surface likely fell below the XRD detection limit.

Representative SEM micrographs of the as-sintered 5 and 10 mol% $Nd_2O_3$-YSZ ceramics are provided in Fig. 6. The amounts of neodymium in the matrix were slightly lower (3 and 7 mass% for the 5 and 10 mol% $Nd_2O_3$-YSZ ceramics, respectively) than the expected theoretical values as seen in Table 5. This was attributed to the presence of the Nd-rich clusters and agglomerates, as indicated by region 'II' of Fig. 6. Linescan analysis shown in Fig. 7 across these agglomerates revealed that Nd was diffusing into the matrix, indicating that the selected SPS parameters allowed for the sufficient interdiffusion between the zirconia matrix and the $Nd_2O_3$ additive.

After degradation testing, the Nd-rich agglomerations disappeared, and an increase in porosity was observed, as seen in Fig. 8. This suggests that supercritical water exposure may cause preferential dissolution of the Nd-rich agglomerates, though further studies are required to confirm these results. SEM-XEDS analysis of the degraded matrix revealed that the Nd content remained within 1% of the as-sintered value, as shown in Table 6 (region 'III'). This suggested that diffusion of Nd from the matrix during supercritical water exposure was not significant.

Similar studies performed by Salehi et al. (Ref 24) also reported improved degradation resistance of YSZ ceramics doped with $Nd_2O_3$ additions. Salehi et al. (Ref 24) suggested that this behavior was related to the increase in cell dimensions of the stabilized tetragonal phase, attributed to the incorporation

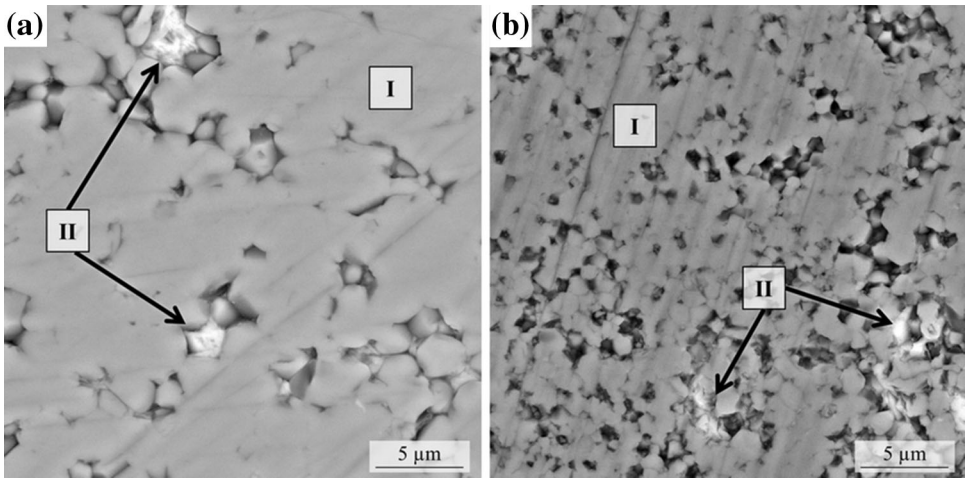


**Fig. 6** SEM micrographs of a) 5 mol% $Nd_2O_3$-YSZ and b) 10 mol% $Nd_2O_3$-YSZ ceramics before degradation testing

**Table 5 Chemical analysis of the as-sintered matrix in the $Nd_2O_3$-YSZ ceramics**

| | | Composition (a) mass% | | | | | |
|---|---|---|---|---|---|---|---|
| **Sample** | **Region** | **Zr** | **O** | **Y** | **Nd** | **Hf** | **Cl** |
| 5 mol% $Nd_2O_3$-YSZ | Theoretical | 56.0 | 24.0 | 9.7 | 10.3 | … | … |
| | I | 62.6 ± 1.5 | 19.1 ± 1.5 | 9.3 ± 0.8 | 7.5 ± 0.8 | 1.6 ± 0.2 | 0.1 ± 0.1 |
| | II | 22.3 ± 8.8 | 9.5 ± 1.7 | 5.2 ± 0.8 | 50.0 ± 6.8 | 0.5 ± 0.4 | 12.3 ± 3.2 |
| 10 mol% $Nd_2O_3$-YSZ | Theoretical | 49.5 | 22.9 | 8.6 | 19.0 | … | … |
| | I | 56.1 ± 1.2 | 21.0 ± 1.8 | 8.9 ± 0.3 | 12.8 ± 0.9 | 1.0 ± 0.2 | 0.1 ± 0.1 |
| | II | 21.2 ± 4.6 | 11.4 ± 2.6 | 4.4 ± 0.7 | 50.2 ± 5.8 | 0.5 ± 0.3 | 12.6 ± 1.6 |

(a) Error shown taken from the standard deviation

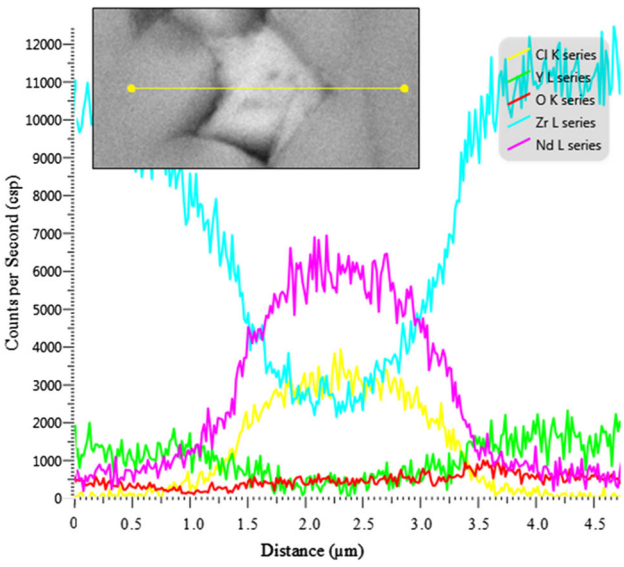


**Fig. 7** Linescan across a Nd-rich agglomerate in the matrix of the as-sintered 5 mol% $Nd_2O_3$-YSZ ceramic

of larger $Nd^{3+}$ ions in the lattice (where the ionic radius for the $Nd^{3+}$ and $Y^{3+}$ ions is 1.109 and 1.019 Å, respectively). The increased unit cell dimension lowered the tetragonal-to-monoclinic transformation temperature, because the internal strain applied to the lattice due to oxygen overcrowding was reduced. Salehi et al. (Ref 24) further suggested that during oxygen annihilation, the larger lattice parameters accommodated the residual tensile stresses which are applied to the lattice during the diffusion of $OH^-$ ions.

### 3.5 Solution Analysis

Retrieved solutions after supercritical water degradation testing of the YSZ and $Nd_2O_3$-YSZ ceramics exhibited distinct white and red colorations, respectively, as seen in Fig. 9. ICP-MS analysis revealed that all retrieved solutions contained both $Y^{3+}$ and $Zr^{4+}$ ions. However, the red colored solutions also contained $Nd^{3+}$ ions, as listed in Table 7. With the increasing $Nd_2O_3$ content in the ceramic, the amount of $Nd^{3+}$ in the solution increased. These results suggest that the dissolved Nd-rich agglomerations went into the supercritical water during testing. Unfortunately, due to solution acidification, formation of precipitates, dissolution of ceramic remnants or the through evaporation of compounds may have occurred. As a result, the absolute quantitative amounts of ionic products may have varied. Furthermore, the retrieved solutions may have been contaminated by degradation products from the 316L steel vessels, despite their passivation and ultrasonic cleaning. Thus, the ICP-MS results provide qualitative results for detection of solutes in the retrieved solutions.

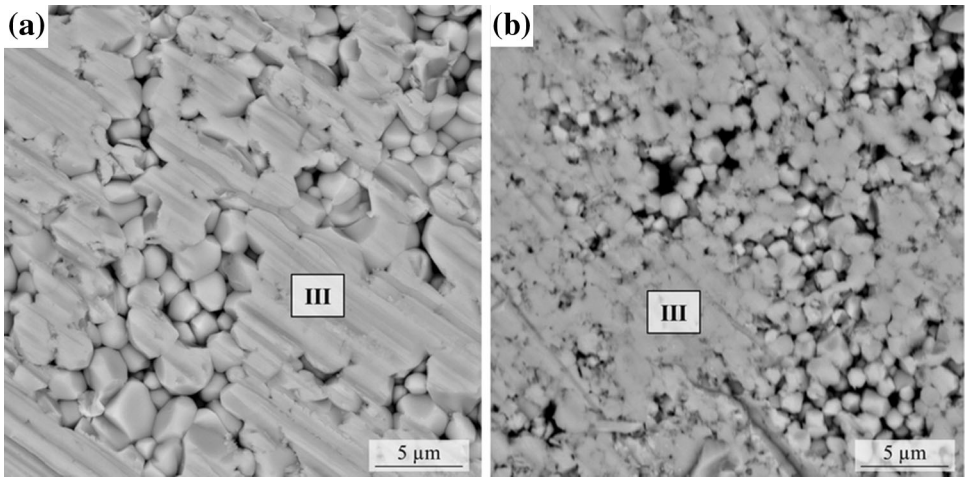


**Fig. 8** SEM micrographs of a) 5 mol% $Nd_2O_3$ and b) 10 mol% $Nd_2O_3$ after degradation testing

**Table 6 Chemical analysis of the degraded microstructure of the $Nd_2O_3$-YSZ ceramics**

| | | Composition (a) mass% | | | | | |
|---|---|---|---|---|---|---|---|
| **Sample** | **Region** | **Zr** | **O** | **Y** | **Nd** | **Hf** | **Cl** |
| 5 mol% $Nd_2O_3$-YSZ | Theoretical | 56.0 | 24.0 | 9.7 | 10.3 | … | … |
| | III | 57.8 ± 2.8 | 25.8 ± 3.8 | 8.8 ± 1.0 | 6.7 ± 1.0 | 1.0 ± 0.3 | 0.0 ± 0.0 |
| 10 mol% $Nd_2O_3$-YSZ | Theoretical | 49.5 | 22.9 | 8.6 | 19.0 | … | … |
| | III | 54.2 ± 2.2 | 24.9 ± 3.1 | 8.3 ± 0.7 | 11.6 ± 0.8 | 1.1 ± 0.3 | 0.0 ± 3e−2 |

(a) Error shown taken from the standard deviation

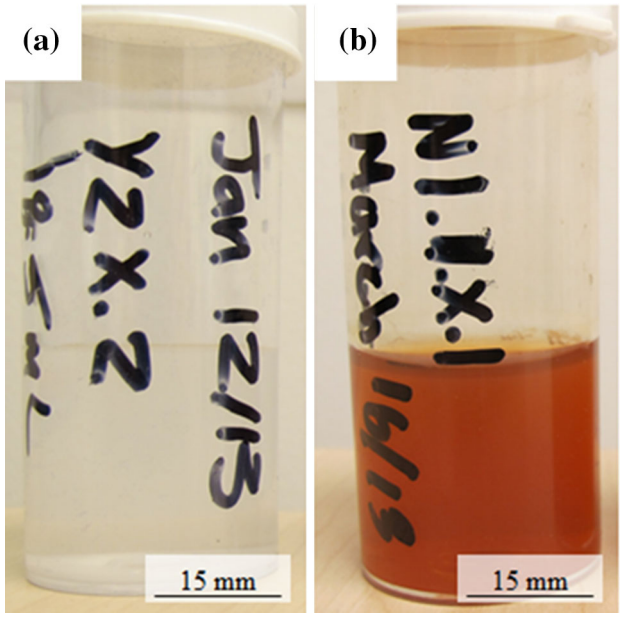


**Fig. 9** Retrieved solutions after supercritical water degradation testing: a) YSZ and b) $Nd_2O_3$-YSZ ceramics

**Table 7 ICP-MS results from solutions retrieved after degradation testing**

| | Element concentration (ppb) | | |
|---|---|---|---|
| **Sample** | **$Zr^{4+}$** | **$Y^{3+}$** | **$Nd^{3+}$** |
| YSZ | 0.2 | 9 | … |
| 5 mol% $Nd_2O_3$-YSZ | 57 | 132 | 2237 |
| 10 mol% $Nd_2O_3$-YSZ | 60 | 485 | 14,189 |

## 4. Conclusion

In this work, the 8 mol% YSZ ceramics with the addition of 0, 5, and 10 mol% of $Nd_2O_3$ were fabricated via SPS processing. Weight losses and microstructural evolutions of the as-sintered specimens were evaluated before and after SCW exposure. The findings of this work are as follows:

- $Nd_2O_3$ additions to YSZ hindered the grain growth and densification during SPS processing.
- Additions of $Nd_2O_3$ to YSZ prevented the undesirable phase transformations during degradation testing, and this

was suggested to be due to the large ionic radii of the incorporated $Nd^{3+}$ ions, which increased the unit cell dimension, lowering the tetragonal-to-monoclinic transformation temperature.

Dissolution of Nd-rich agglomerates found in the as-sintered $Nd_2O_3$-YSZ ceramics occurred during supercritical water exposure.

Nd-rich bands in the 10 mol% $Nd_2O_3$-YSZ ceramic likely contributed to material cracking and spallation during degradation testing, which was associated to the mismatch in the thermal expansion between the bands and the YSZ matrix.

## Acknowledgments

The authors wish to thank Prof. E. Asselin from the University of British Columbia for his valuable help in developing the degradation testing procedure; Mr. D. Arkinstall for his assistance in SEM characterization, as well as Prof. B.S. Murty, Mr. K. Akkiraju, and Mr. S. Ipe Varghese from the Indian Institute of Technology, Madras for their assistance with SPS processing. The authors would also like to thank NSERC-SPG program for funding this research.

## References

1. P. Kritzer, Corrosion in High-Temperature and Supercritical Water and Aqueous Solutions: A Review, *J. Supercrit. Fluids*, 2004, **29**(1), p 1–29
2. Nuclear Energy Research Advisory Committee and the Generation IV International Forum, "A Technology Roadmap for Generation IV Nuclear Energy Systems," Department of Energy - Office of Scientific and Technical Information, (2002)
3. International Energy Agency and Nuclear Energy Agency, 2010. Technology roadmap nuclear energy," [online]. http://www.iea.org
4. C. Sun, R. Hui, W. Qu, and S. Yick, Progress in Corrosion Resistant Materials for Supercritical Water Reactors, *J. Corros. Sci.*, 2009, **51**(11), p 2508–2523
5. C. K. Chow, S. J. Bushby and H. F. Khartabil, A Fuel Channel Design for CANDU-SCWR, *Proceedings of the 14th International Conference on Nuclear Engineering*, Miami, FL, 2006
6. S. Ho, On the Structural Chemistry of Zirconium Oxide, *Mat. Sci. Eng.*, 1982, **54**(1), p 23–29
7. O. Graeve, Zirconia, *Ceramics and Glass Materials: Structure, Properties and Processing*, J. F. Shackelford and R. H. Dormeus, Eds., Springer, New York, NY, 2008, p 169–197
8. P. Li, I.W. Chen, and J.E. Penner-Hahn, Effect of dopants on zirconia Stabilization—An X-ray Absorption Study: II, Tetravalent Dopants, *J. Am. Ceram. Soc.*, 1994, **77**(5), p 1281–1288
9. P. Li, I.W. Chen, and J.E. Penner-Hahn, Effect of Dopants on Zirconia Stabilization—An X-ray Absorption Study: I, Trivalent Dopants, *J. Am. Ceram. Soc.*, 1994, **77**(1), p 118–128
10. S. Fabris, A.T. Paxton, and M.W. Finnis, A Stabilization Mechanism of Zirconia Based on Oxygen Vacancies Only, *Acta Mater.*, 2002, **50**(20), p 5171–5178
11. S.B. Bhaduri, Science of Zirconia-Related Engineering Ceramics, *Sãdhanã-Acad Proc. Eng. Sci.*, 1988, **13**(1-2), p 97–117
12. R.D. Shannon, Revised Effective Ionic Radii and Systematic Studies of Interatomic Distances in Halides and Chalocogenides, *Acta Crystallogr. A*, 1976, **32**(5), p 751–767
13. J. Chevalier, L. Gremillard, A.V. Virkar, and D.R. Clarke, The Tetragonal-Monoclinic Transformation in Zirconia: Lessons Learned and Future Trends, *J. Am. Ceram. Soc.*, 2009, **92**(9), p 1901–1920
14. F.F. Lange, G.L. Dunlop, and B.I. Davis, Degradation During Aging of Transformation Toughened $ZrO_2$-$Y_2O_3$ Materials at 250 °C, *J. Am. Ceram. Soc.*, 1986, **69**(3), p 237–240
15. J.A. Muñoz Tabares, E. Jimenez-Pique, and M. Anglada, Subsurface Evaluation of Hydrothermal Degradation of Zirconia, *Acta Mater.*, 2011, **59**(2), p 473–484
16. J. Eichler, J. Rodel, U. Eisele, and M. Hoffman, Effect of Grain Size on Mechanical Properties of Submicrometer 3Y-TZP: Fracture strength and Hydrothermal Degradation, *J. Am. Ceram. Soc.*, 2007, **90**(9), p 2830–2836
17. J. Muñoz-Saldaña, H. Balmori-Ramfrez, D. Jaramillo-Vigueras, T. Iga, and G. Schneider, Mechanical Properties and Low-Temperature Aging of Tetragonal Zirconia Polycrystals Processed by Hot Isotactic Pressing, *J. Mater. Res.*, 2003, **18**(10), p 2415–2426
18. S. Lawson, Environmental Degradation of Zirconia Ceramics, *J. Eur. Ceram. Soc.*, 1995, **15**(6), p 485–502
19. T. Duong, A.M. Limarga, and D.R. Clarke, Diffusion of Water Species in Yttria Stabilized Zirconia, *J. Am. Ceram. Soc.*, 2009, **92**(11), p 2731–2737
20. X. Guo and T. Schober, Water Incorporation in Tetragonal Zirconia, *J. Am. Ceram. Soc.*, 2004, **87**(4), p 746–748
21. X. Guo, Low Temperature Degradation Mechanism of Tetragonal Zirconia Ceramic in Water: Role of Oxygen Vacancies, *Solid State Ionics*, 1998, **112**(1), p 113–116
22. X. Guo, On the Degradation of Zirconia Ceramics During Low-Temperature Annealing in Water or Water Vapor, *J. Phys. Chem. Solids*, 1999, **60**(4), p 539–546
23. T. Duong, A.M. Limarga, and D.R. Clarke, Diffusion of Water Species in Yttria-Stabilized Zirconia, *J. Am. Ceram. Soc.*, 2009, **92**(11), p 2731–2737
24. S.A. Salehi, K. Vanmeensel, A.K. Swarnakar, O. Van der Biest, and J. Vleugels, Hydrothermal Stability of Mixed Stabilized Tetragonal (Y, Nd)-$ZrO_2$ Ceramics, *J. Alloys Compd.*, 2010, **495**(2), p 556–560
25. T. Xu, J. Vleugels, O. Van der Biest, Y. Kan, and P. Wang, Phase Stability and Mechanical Properties of TZP with Low Mixed Nd2O3/Y2O3 Stabiliser Content, *J. Eur. Ceram. Soc.*, 2006, **26**(7), p 1205–1211
26. M. Mulukutla, A. Singh, and S.P. Harimkar, Spark Plasma Sintering for Multi-Scale Surface Engineering of Materials, *J. Mater.*, 2010, **62**(6), p 65–71
27. R. Orrú, R. Licheri, A. M. Locci, A. Cincotti, and G. Cao, Consolidation/Synthesis of Materials by Electric Current Activated/Assisted Sintering, *Mat. Sci. Eng. R*, 2009, **63**(4), p 127–287
28. S.G. Huang, K. Vanmeensel, O. Van der Biest, and J. Vleugels, Influence of $CeO_2$ Reduction on the Microstructure and Mechanical Properties of Pulsed Electric Current Sintered $Y_2O_3$-$CeO_2$ Co-stabilized $ZrO_2$ Ceramics, *J. Am. Ceram. Soc.*, 2007, **90**(3), p 1420–1426
29. A. Siebert-Timmer K. Mondal and L. Bichler, Degradation of SPS Fabricated YSZ and $CeO_2$-YSZ Ceramics in Supercritical Water, *Int. J. Applied Ceram. Technol.* doi:10.1111/ijac.1234
30. *ASTM Standard G31-72: Standard Practice for Laboratory Immersion Corrosion Testing of Metals*, ASTM International, West Conshohocken, PA, 2004
31. U. Anselmi-Tamburini, J.E. Garay, and Z.A. Munir, Spark Plasma Sintering and Characterization of Bulk Nanostructured Fully Stabilized Zirconia: Part I, Densification Studies, *J. Mater. Res.*, 2004, **19**(11), p 3255–3262
32. P. Dahl, I. Kaus, Z. Zhao, M. Johnsson, M. Nygren, K. Wiik, T. Grande, and M.A. Einarsrud, Densification and Properties of Zirconia Prepared by Three Different Sintering Techniques, *Ceram. Int.*, 2007, **33**(8), p 1603–1610
33. C. Verdon, *Development and Characterization of Yttria Stabilized Zirconia Doped with Erbia*, University of British Columbia, Kelowna, BC, 2012
34. S. Stephan and J. William, Thermal Expansion and Phase Inversion of Rare-earth Oxides, U.S. Dept. of the Interior Bureau of Mines, WA, Rep. 5747, 1961
35. H. Hayashi, T. Saitou, N. Maruyama, H. Inaba, K. Kawamura, and M. Mori, Thermal Expansion Coefficient of Yttria Stabilized Zirconia for Various Yttria Contents, *Solid State Ionics*, 2005, **176**(5), p 613–619
36. R.D. Shannon, Revised Effective Ionic Radii and Systematic Studies of Interatomic Distances in Halides and Chalocogenides, *Acta Crystallogr. A*, 1976, **32**(5), p 751–767
37. H.G. Scott, Phase Relationships in the Zirconia-Yttria System, *J. Mater. Sci.*, 1975, **10**(9), p 1527–1535
38. J.A. Krogstad, M. Lepple, Y. Gao, D.M. Lipkin, and C.G. Levi, Effect of Yttria Content on the Zirconia Unit Cell Parameters, *J. Amer. Ceram. Soc.*, 2011, **94**(12), p 4548–4555